A Comparison of Modal Decomposition Methods Applied to Hypersonic Schlieren Video

Arman C. Ghannadian*, Ryan Gosse†, and Subrata Roy ‡
University of Florida, Gainesville, Florida, 32611, USA

Zachary D. Lawless§ and Joseph S. Jewell¶
Purdue University, West Lafayette, IN, 47907

The modal decomposition methods formulate the governing equations of a system as a linear combination of the various modes to provide a powerful means for examining the influence of any individual or combined modes of interest. They are commonly used to characterize complex signal dominated fluid flows and their control. Three modal decomposition techniques, namely, the proper orthogonal decomposition (POD), dynamic mode decomposition (DMD), and higher-order dynamic mode decomposition (HODMD), are studied to understand their ability to analyze a high-speed schlieren video for Mach 6 flow over a cone. The video is focused on the base of the cone and the base flow region. The data-driven modal analysis techniques are used to analyze the interference generated by the sting on the base flow region. The basic characteristics of the base flow were under investigation in the experiment, so it was desirable to gain insight into the impact that the presence of the sting has on the base flow. The POD, DMD, and HODMD methods give different insights into the sting interference, but all three methods appear to show that the disturbance originating from the sting appears in the base region of the cone.

I. Nomenclature

Symbols	Description
a	POD time coefficient
b	DMD/HODMD mode amplitudes
d	Delay parameter for HODMD
R	System matrix
r	Truncated SVD rank
$\hat{R}$	Reduced system/Koopman matrix
$\tilde{R}$	Modified Koopman matrix
$\bar{R}$	Reduced modified Koopman matrix
S	HOSVD core tensor
T	HOSVD temporal mode/snapshot matrix
$\tilde{T}$	Modified HOSVD snapshot matrix
$\bar{T}$	Reduced modified HOSVD snapshot matrix
t	Time
U, M	Matrices containing singular vectors
V	Snapshot matrix or tensor
W	Reduced system eigenvector matrix
X, Y	HOSVD spatial mode matrices
Greek Symbols	
δ	Growth rate
ε	RRMSE tolerance
λ	DMD/HODMD eigenvalue
Λ	DMD/HODMD eigenvalue matrix
ω	Angular frequency
ψ	POD mode
Ψ	POD mode matrix
ϕ	DMD/HODMD mode
Φ	Dynamic mode matirx
Σ	Singular value matrix
σ	Singular value
Abbreviations	
DMD	Dynamic mode decomposition
HODMD	Higher-order dynamic mode decomposition
HOSVD	Higher-order singular value decomposition
RRMSE	Relative root mean square error
SVD	Singular value decomposition
POD	Proper orthogonal decomposition
Subscripts	
i, j	Spatial dimension indices
k	Temporal index

II. Introduction

THE complex nature of the physics involved in high-speed aerodynamics requires expensive numerical simulation validated by detailed experimental investigation. At high speeds, the flow produces thin boundary layers that are

*PhD Student, Department of Mechanical and Aerospace Engineering, AIAA Student Member. ghannadian.arman@ufl.edu
†Professor of Practice, Florida Applied Research in Engineering, AIAA Associate Fellow. ryan.gosse@ufl.edu
‡Professor, Department of Mechanical & Aerospace Engineering, AIAA Associate Fellow. roy@ufl.edu
§Graduate Research Assistant, School of Aeronautics and Astronautics, AIAA Student Member. zlawless@purdue.edu
¶John Bogdanoff Associate Professor, School of Aeronautics and Astronautics, AIAA Associate Fellow. jsjewell@purdue.edu

sensitive to high-frequency acoustic perturbations. Traditional sensors such as high-frequency pressure transducers can measure these perturbations but often do not give a complete picture of the physical processes acting on the disturbances. Simple theories exist for laminar flow states where acoustic noise grows through linear processes. As the flow becomes chaotic and complex, large eddy simulation (LES) or direct numerical simulation (DNS) computational fluid dynamics (CFD) simulations are required to provide fundamental insight numerically.

Modal decomposition techniques are commonly used in the field of fluid mechanics to characterize complex or turbulent flows. Among modal decomposition techniques, the proper orthogonal decomposition (POD), dynamic mode decomposition (DMD), and their variants are some of the most widely used. Modes can be extracted from any unsteady data stream allowing analysis to be applied to experimental or computational data. In addition, data from a wide variety of physical systems can be analyzed in the same way. For example, DMD and POD have been applied successfully in various fields from fluid dynamics to neuroscience [1]. The detachment of these methods from the governing physics also allows for the decomposition of flow visualization data such as schlieren video to be used in analyzing the underlying physics. However, care must be taken in the acquisition of data as well as in interpreting the physical significance of the modes

For POD and DMD, the data $V(x_i, t_k)$ is initially organized as a snapshot matrix V_{ik} with columns $\mathbf{v}(t_k)$ containing data at each time step. The POD, which was originally introduced in the 1960s to the fluid dynamics community to study turbulence [2], represents this discrete data as

$$V(x_i, t_k) = \sum_{n=1}^{N} a_n(t_k)\psi_n(x_i), \tag{1}$$

where $a_n(t_k)$ are the time coefficients and $\psi_n(x_i)$ are the spatial POD modes. It should be briefly noted that the focus of this work is the space-only POD whose modes consist of deterministic spatial functions modulated by random time coefficients [3]. Space-time formulations lead to other methods like spectral POD (SPOD) which finds single-frequency modes that are coherent in both space and time. The goal of the POD remains the same, to optimally capture the variance or energy of an ensemble of a stochastic process. The POD method does this by computing modes as eigenvectors of the autocovariance matrix and ranking them according to energy content.

The DMD method was developed by Schmid in 2008 [4, 5]. In a standard DMD analysis, data sets representing dynamic systems are written as

$$\mathbf{v}(t_k) \approx \mathbf{v}_{\mathrm{DMD}}(t_k) \equiv \sum_{n=1}^{N} b_n \boldsymbol{\phi}_n \mathrm{e}^{(\delta_n + i\omega_n)t_k}, \tag{2}$$

where b represents the mode amplitude and $\boldsymbol{\phi}$ represents the DMD mode vector. Both the amplitudes and modes are generally complex-valued for standard DMD. The exponential term describes the system's evolution in time, δ is the temporal growth rate and ω is the angular frequency [4]. The modes are eigenvectors of a matrix R which is defined to be the best-fit matrix solution that advances the data over the entire domain at an instant (a snapshot) one time step into the future. The frequencies and growth rates are computed from the eigenvalues of this matrix. Each mode has a single growth rate and frequency associated with it. This differs from POD because POD mode time coefficients can contain multiple frequencies, although for stationary stochastic processes, the SPOD can be used to express temporal correlation among resolved structures that exhibit the optimality of POD. Additionally, since the DMD algorithm has the benefit of finding the growth rates of each mode, stability can be analyzed. Due to Eq. (2), non-zero frequency modes must come in complex-conjugate pairs if real data is represented.

There are many variants of DMD that attempt to improve noise robustness [4, 6], and HODMD is the one used in this analysis. Le Clainche and Vega first developed the HODMD method in 2017 [7]. For HODMD, the data is expanded similarly to Eq. (2), but the expansion is generalized to data sets organized as higher-order tensors. For example, a third-order tensor could be represented as

$$V_{ijk} \approx \sum_{n=1}^{N} b_n \phi_{ijn} \mathrm{e}^{(\delta_n + i\omega_n)t_k}. \tag{3}$$

Here, the eigenvectors come from a matrix relating a single snapshot to d snapshots rather than just the snapshot at the next time step as is the case with standard DMD. This will be expanded upon in section III.C. Another difference is that i and j correspond to different spatial dimensions, whereas standard DMD stacks all the spatial information into a single index. This allows for better control over noise removal and leads to a further extension of the method to obtain expansions in both space and time with wave number and spatial growth rate in addition to frequency and temporal growth rate, referred to as spatio-temporal Koopman decomposition (STKD) [8]. Another benefit of HODMD is that it handles situations with higher temporal complexity than spatial complexity better than standard DMD [7]. This is a result of the fact that HODMD uses time-delayed snapshots that allow for the complex-conjugate pair of eigenvectors/eigenvalues necessary for representing a temporal frequency to be computed even when the corresponding spatial modes do not increase the rank of the set of HODMD modes.

In this paper, we review the algorithms for POD, DMD, and HODMD and apply them to schlieren video of Mach 6 flow past a cone. We show preliminary results for an analysis of the effect of sting interference on the base flow of the cone as the interference convects downstream. The experiment investigated the base flow of a hypersonic cone because hypersonic flight vehicles in the Mach 5-10 range experience a significant amount of base drag [9]. In order to tackle the problem of base drag, a fundamental investigation into the base flow is necessary. Therefore, the effects of experimental phenomena such as sting interference on the base flow are important to characterize. This could, for example, modify mixing in the shear layer that bounds the recirculation region. The spatial modes and DMD spectra are shown from an initial analysis. We use the analysis of this sting interference to compare the insights, advantages, and disadvantages the modal decomposition techniques offer in the analysis of flow-visualization data in general as well as the effect of sting interference on the base flow of the experiment being analyzed.

III. Methodology

The geometry is labeled in Fig. 1 below, which shows the first frame of the video. The geometry is a 7 deg. half-angle blunted cone with a tip radius of 16μm and a base diameter of 4.31 inches. The tunnel was operated at initial stagnation pressures and temperatures of 100 psia and 153.1°C, respectively. The schlieren setup is a standard z-type schlieren that consists of two 8-inch parabolic mirrors that direct light through optical grade sapphire windows[10, 11]. The experiment was carried out in the Boeing/AFOSR Mach 6 Quiet Tunnel (BAM6QT) at Purdue University, a low-disturbance facility with freestream pitot pressure noise levels of 0.02% RMS or lower [12]. This schlieren configuration has been used in BAM6QT to measure transient fluid effects including boundary layer instability growth[13–15], recirculation bubble unsteadiness [16–19], and hypersonic inlet shock wave-boundary layer interaction [20].

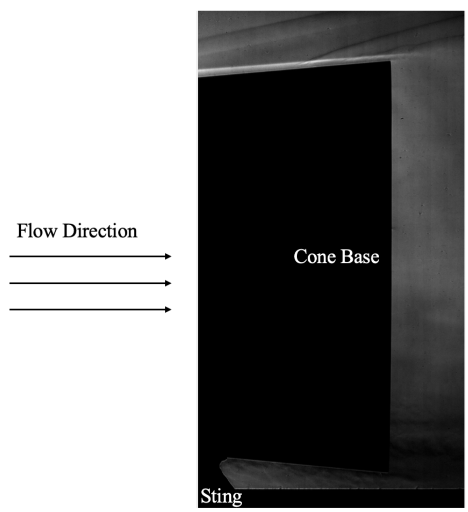

Fig. 1 First frame/snapshot of video data.

The video is zoomed in to the base region of the cone. For both POD and standard DMD, the schlieren video is organized into snapshot matrices. This is done by taking each frame of the video as a matrix of grayscale pixel values and reshaping it into a column of the snapshot matrix. Thus,

$$V_{ik} = V(x_i, t_k), \tag{4}$$

where the i index contains pixel information along both spatial dimensions of the video. For HODMD, the video frames are left as matrices and stacked into a third-order snapshot tensor, V_{ijk}, as shown in Fig. 2 below. It should be noted that the orientation of the video in Fig. 2 differs from Fig. 1 because Fig. 2 shows how the video was originally oriented while Fig. 1 was changed to show the more traditional perspective of flow moving from left to right. The video used in the preliminary analysis was captured at 100 kHz and 1000 snapshots were used in the analysis.

All three of these algorithms were implemented in MATLAB. Both POD and DMD results were compared to the results for a Reynold's number of 100 for a flow past a cylinder from [4], using the data set from [21]. The HODMD spectrum was compared with the standard DMD spectrum for the cylinder case for verification.

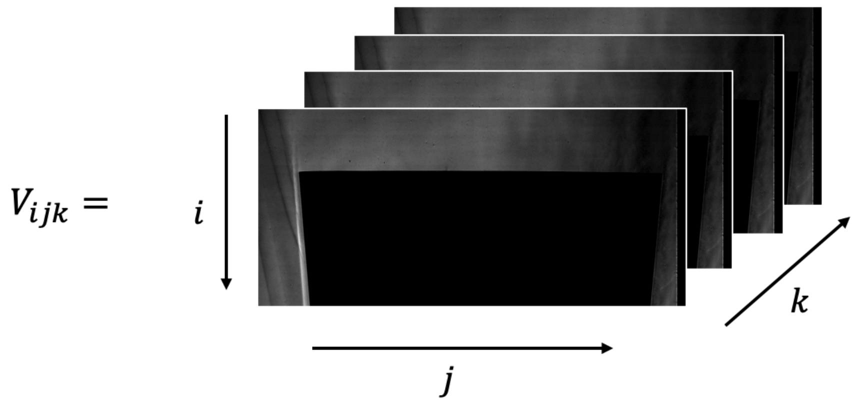

Fig. 2 Organization of schlieren video as a third-order tensor. This data is oriented differently than in Fig. 1 because this orientation is how the video frames were initially organized.

Finally, before applying the methods, the video was cropped to the region of interest depicted below in Fig. 3 in order to capture the sting effect more closely. This is because it is evident when watching the schlieren video, that the bottom half of the base flow region is darker and appears to contain some kind of unsteady fluctuation not apparent in the top half. Additionally, it is expected that the disturbance would be confined to the bottom half of the base flow due to the physics of the problem. The recirculation region results in downward-moving air at the bottom half of the cone base which counters the advancement of the disturbance across the centerline. If the dynamics of interest are not in the top half of the video frame then it is undesirable to compute modes that capture the desired dynamics and additional dynamics not of interest simultaneously. This saves computational time as well.

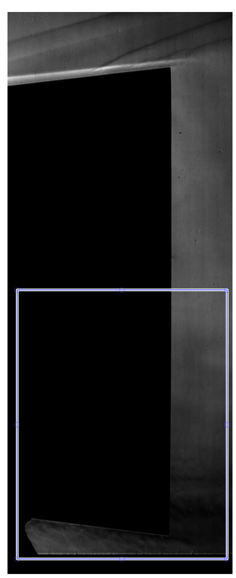

Fig. 3 Region of interest for analysis.

A. POD of Schlieren Video

Here, we use the singular value decomposition (SVD) approach for performing POD [2, 4]. The video is read as a series of matrices of pixel values representing a series of video frames. Pixel values for each frame at a specific time are stacked into a single column of a new matrix referred to as the snapshot matrix. The goal is to represent this time-series of data as Eq. (1). Taking the singular value decomposition of the mean-subtracted snapshot matrix, we have

$$V = U\Sigma M^*, \tag{5}$$

where U and M are left and right singular vector matrices, respectively [4]. The asterisk in the superscript denotes the conjugate transpose. The columns of these matrices are the left and right singular vectors, $\mathbf{u}$ and $\mathbf{m}$, respectively. The matrix Σ contains singular values on the diagonal, which are the square roots of the eigenvalues of VV^*. The left singular vectors (U) give the POD modes, so that

$$\Psi = U. \tag{6}$$

The time coefficients can be given as the product of the singular values and the rows of the right singular vector matrix. This connection is made more clear by rewriting Eq. (5) as

$$V = \sum_{n=1}^{N} \mathbf{u}_n(x)\sigma_n\mathbf{m}_n^*(t), \tag{7}$$

where σ_n are the singular values that are related to the mode energy. Here, in the analysis of schlieren video, modal energy is related to the variance of the density gradient rather than kinetic energy which would be the case if velocity data was being used. This recovers Eq. (1).

The SVD gives the POD modes because it gives the optimal representation of the data given N modes by maximizing the amount of energy captured by solving for the singular vectors and singular values of the snapshot matrix [2]. Thus, truncating the SVD matrices to rank r will minimize the error for the lower rank representation. Additionally, the singular vectors are orthogonal so that the columns of U contain only spatial correlations while the columns of M contain only temporal correlations, each of which depends on only one mode [2, 4].

A downside to POD is that many modes can be required to capture dynamics of interest if many of the snapshots have small but unique spatio-temporal fluctuations. This can be the case with noisy data as the noise increases the temporal complexity, especially if the desired dynamics are on the same order as the noise levels. This can lead to many POD modes with very small singular values and multiple frequencies in the associated time dynamics. The flow is then decomposed into a sum of a great number of low-energy modes so that the importance of each mode can be difficult to decipher. Then, removing noise by eliminating low-energy modes will potentially result in eliminating low-energy high temporal complexity dynamics that may be desirable to keep. Thus, energy alone may not always be the optimal criterion for mode organization for this spatial POD where the modes are only functions of space and do not necessarily exhibit temporal coherence. The benefit of DMD and its higher-order extension is the organization of modes based on dynamical relevance (via a least-squares fitting) and frequency, though the modes are not necessarily optimal in capturing energy. The SPOD method also finds single-frequency modes that do satisfy this property. In fact, in [3] the SPOD modes are shown to be optimally averaged DMD modes. However, the HODMD and DMD have several more advantages. Namely, they are suitable for nonstationary dynamics, and the HODMD method allows for spatio-temporal expansions (STKD) [8] that can decouple and simultaneously describe evolution in individual spatial dimensions and time.

B. DMD of Schlieren Video

A full description of the DMD method can be found in [4]. We focus on a short summary with application to schlieren video analysis. For an $I \times K$ snapshot matrix, which is the same snapshot matrix of pixel values used for the POD analysis, the time between snapshots Δt is related to the current time as

$$t_k = (k-1)\Delta t. \tag{8}$$

The snapshot matrix is divided into V_1, which takes the first through $K-1$ columns of V, and V_2, which takes the second through K^{th} columns of V. The columns of V must be spaced out evenly in time so that Δt is constant. Then, for some matrix R,

$$V_2 \approx RV_1. \tag{9}$$

The matrix R is defined as

$$R \equiv V_2 V_1^+, \tag{10}$$

and the + in the superscript denotes the pseudo-inverse. With this definition for R as the best-fit matrix satisfying Eq. (9), $\boldsymbol{\phi}_n$ are the eigenvectors of R. The growth rates and frequencies are then

$$\delta_n + i\omega_n = \frac{\ln(\lambda_n)}{\Delta t}, \tag{11}$$

where λ_n are the eigenvalues of R corresponding to $\boldsymbol{\phi}_n$.

In general, R is a large matrix of size $I \times I$, but the eigenvalues and eigenvectors of R can be found from the eigenvalues and eigenvectors of a reduced matrix $\hat{R}$, given by

$$\hat{R} = U^* V_2 M \Sigma^+. \tag{12}$$

Here U and M are matrices of left and right singular vectors from an SVD of the X_1 matrix. It is noted that a rank truncation is often performed at this step, keeping only the first r singular values and columns of U and M. If the eigenvectors of $\hat{R}$ are stored as the columns of a matrix W, the modes $\boldsymbol{\phi}_n$ stored in the columns of a matrix Φ, can be obtained as

$$\Phi = V_2 M \Sigma^+ W. \tag{13}$$

The DMD representation of the data can be written as

$$\mathbf{v}_{\mathrm{DMD}}(t_k) = \Phi \Lambda^{k-1} \mathbf{b}. \tag{14}$$

The matrix Φ contains the eigenvectors of R in its columns, Λ is a matrix containing eigenvalues, λ_n, in its diagonal elements, and $\mathbf{b}$ is a vector containing mode amplitudes. Then the amplitudes are solved as

$$\mathbf{b} = \Phi^+ \mathbf{v}(t = 0), \tag{15}$$

which gives the least-squares solution of $\mathbf{b}$ based on the first snapshot.

A downside for the standard DMD in the application to experimental data like schlieren videos is that it can give spurious results for data with higher temporal complexity than spatial complexity. This is often the case with experimental data, and the HODMD algorithm described in the next section exploits time-delayed snapshots to overcome this limitation.

C. HODMD of Schlieren Video

The Multi-dimensional HODMD algorithm [8] is summarized here. The method starts with a higher-order singular value decomposition (HOSVD). The HOSVD decomposes a tensor into matrices of singular vectors corresponding to each dimension separately. The video is organized as a third-order tensor and the HOSVD is applied. This is given below as [22]

$$V_{ijk} \approx \sum_{n=1}^{N} \sum_{p_1=1}^{P_1} \sum_{p_2=1}^{P_2} S_{p_1 p_2 n} X_{i p_1} Y_{j p_2} T_{kn}. \tag{16}$$

Here, T_{kn} is a matrix corresponding to the time dimension, and X and Y correspond to the two spatial dimensions. The tensor $S_{p_1 p_2 n}$ is referred to as the core tensor. The subscripts p correspond to the number of singular values, and a rank-truncation can be performed in each dimension separately to approximate the original snapshot tensor with a relative root mean square error (RRMSE) tolerance, ε [7].

Now, T_{kn} is scaled by the temporal singular values, σ_n^t, so that Eq. (16) can be written as

$$V_{ijk} \approx \sum_{n=1}^{N} \sum_{p_1=1}^{P_1} \sum_{p_2=1}^{P_2} S_{p_1 p_2 n} X_{i p_1} Y_{j p_2} \frac{1}{\sigma_n^t} \hat{T}_{kn}. \tag{17}$$

Additionally, N is reduced to truncate the rank of the temporal modes based on the singular values corresponding to the temporal SVD. The final step is applying the DMD-d algorithm to the rescaled temporal matrix $\hat{T}_{nk}$. The resulting modes are plugged into Eq. (17) in place of $\hat{T}_{kn}$ to obtain the final HODMD modes, ϕ_{ijn}. The DMD-d algorithm alters the standard DMD approximation in Eq. (9) as

$$\mathbf{v}_{k+d} = R_1\mathbf{v}_k + R_2\mathbf{v}_{k+1} + ... + R_d\mathbf{v}_{k+d-1} \tag{18}$$

for $k = 1, ..., k + d$ [22]. Following [22], Eq. (18) is rewritten for the rescaled temporal modes $\hat{T}$ as

$$\hat{T}_{d+1}^{K} \approx \hat{R}_1\hat{T}_1^{K-d} + \hat{R}_2\hat{T}_2^{K-d+1} + ... + \hat{R}_d\hat{T}_d^{K-1}, \tag{19}$$

where the original temporal mode matrix has been divided into d blocks of size $k - d$. The superscript index signifies the column extent of the matrix block, while the subscript index signifies the first column. For example, T_2^{k-d} would be the matrix block from the 2$^{\text{nd}}$ through $k - d^{\text{th}}$ columns of the matrix T. This is further rewritten as

$$\tilde{T}_2^{K-d+1} = \tilde{R}\tilde{T}_1^{K-d}, \tag{20}$$

where $\tilde{T}$ are referred to as the modified snapshots and $\tilde{R}$ is the modified Koopman matrix [7, 8, 22]. The algorithm proceeds by applying a truncated SVD to the modified snapshot matrix, keeping enough singular values to ensure the RRMSE tolerance is adhered to. Defining $\bar{T}_1^{K-d+1}$ as the product of the new singular value matrix and right singular vectors of the modified snapshots, we can write

$$\bar{T}_2^{K-d+1} = \bar{R}\bar{T}_1^{K-d}. \tag{21}$$

Here, the overbar denotes a reduced modified value so that $\bar{R}$ is the reduced modified Koopman matrix, and the $\bar{T}$ is a reduced modified snapshot matrix. The reduced modified Koopman matrix can be solved for by right multiplying Eq. (21) by the pseudo-inverse of $\bar{T}_1^{K-d}$, and the eigenvectors and eigenvalues of $\bar{R}$ give the reduced HODMD modes and HODMD spectrum [22]. The reduced modes can be substituted into Eq. (17) to construct the full HODMD modes. The amplitudes can be found similarly to the standard DMD mode amplitudes, via a least-squares fit [7]. The amplitudes and modes here are rescaled to obtain real amplitudes and modes with unit RMS norm.

IV. Results and Discussion

This section presents results from the POD, DMD, and HODMD algorithms applied to the video. It should be clarified here that the video frames are 2D slices merging a truly 3D flow-field into a single slice depicting density gradient. Camera focus is used to introduce a weighted bias of a 2D planar assumption. This adds another layer of difficulty in analyzing the modes. Nonetheless, it is still possible to take away some meaning from the results.

A. POD Modes

Each mode contour is a visualization of correlations of the pixel value data related to the density gradient. The POD modes are in descending order in terms of their mode energies, which correspond to the variance of density gradient for schlieren videos. The 9$^{\text{th}}$, 10$^{\text{th}}$, and 13$^{\text{th}}$ modes appear to show an influence of the sting interference on the base region most clearly. The time coefficients $a_{9,\,10,\,13}(t)$ are plotted alongside the associated power spectrum below in Fig. 4 below. The highest peaks in the PSD occur 12.9 kHz, 3.0 kHz, and 0.5 kHz for the 9$^{\text{th}}$ mode and at 9.2 kHz, 5.2 kHz, and 10.3 kHz for the 10$^{\text{th}}$ mode time coefficients. The largest peaks for the 13$^{\text{th}}$ mode occur at frequencies of 6.7 kHz, 4.0 kHz, and 3.6 kHz. All three time coefficient plots have peaks in the 10 kHz, 20 kHz, 30 kHz, and 40 kHz regions with similar gaps between them, likely corresponding to oscillations and their harmonics. These could be related to a vortex shedding-like disturbance pattern traveling from the sting. The POD gives two modes to capture traveling waves similarly to the DMD having a complex conjugate pair, so two sequential modes with peaks at the same frequencies likely represent this. The results are similar to the DMD and HODMD results that will be presented (see Figs. 7 and 10). Figure 5 contains a plot of the POD eigenvalues σ^2 for each mode as well as a PSD contour for the time coefficients 9 to 21.

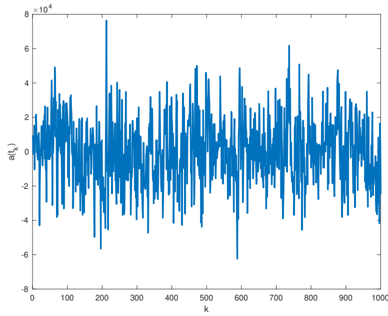

(a) Mode 9 time coefficients.

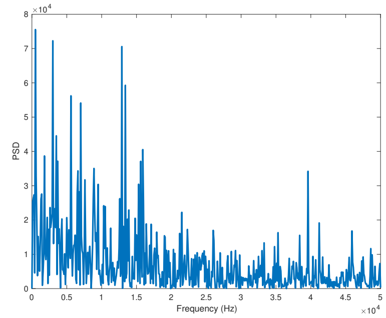

(b) Mode 9 PSD.

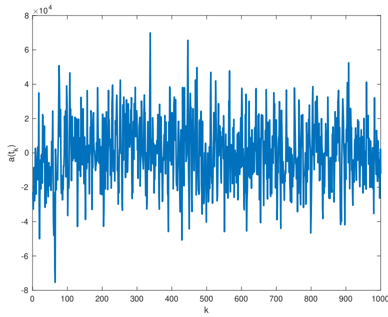

(c) Mode 10 time coefficients.

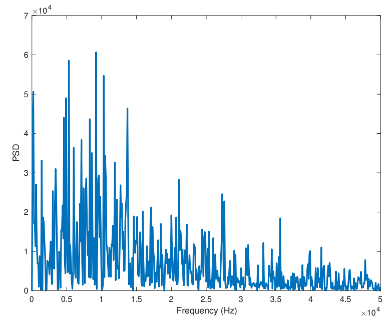

(d) Mode 10 PSD.

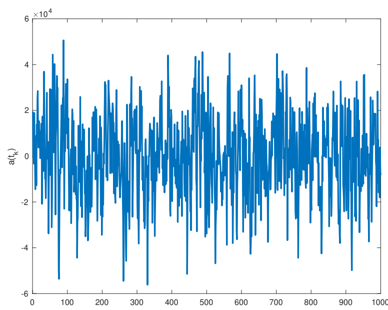

(e) Mode 13 time coefficiens.

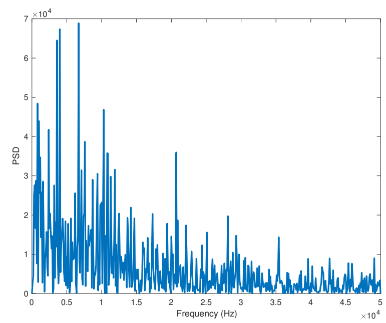

(f) Mode 13 PSD.

Fig. 4 POD mode time coefficients and frequencies.

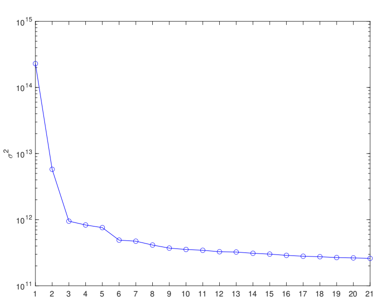

(a)

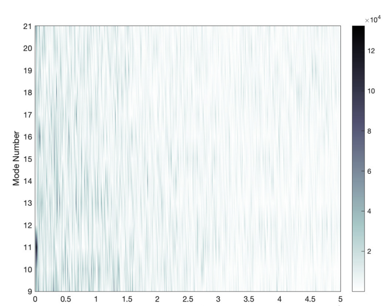

(b)

Fig. 5 POD results: (a) Mode energies; (b) PSD of time coefficients for modes 9 to 21.

The POD modes that most clearly show sting interference are plotted in Fig. 6 below.

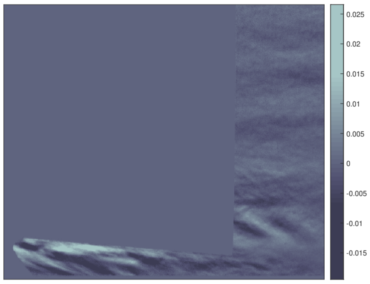

(a) POD mode 9.

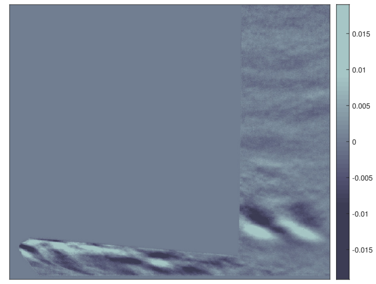

(b) POD mode 10.

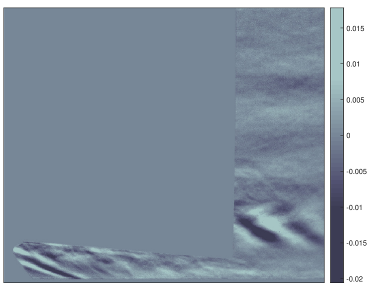

(c) POD mode 13.

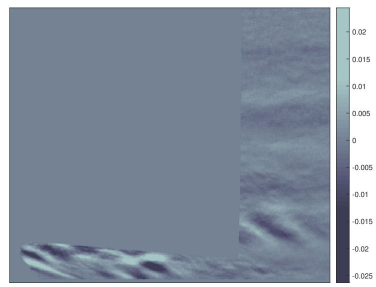

(d) POD mode 14.

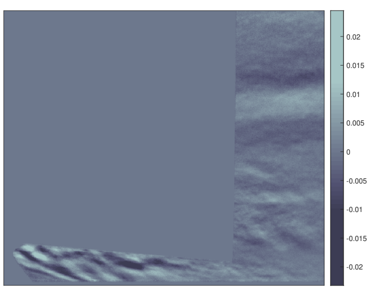

(e) POD mode 16.

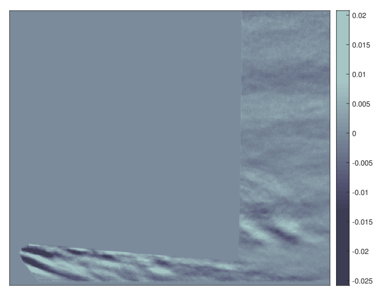

(f) POD mode 17.

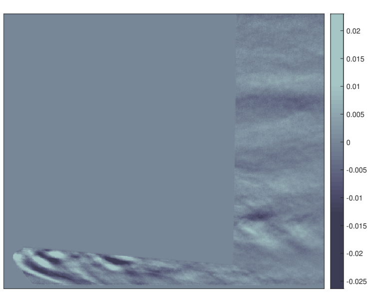

(g) POD mode 18.

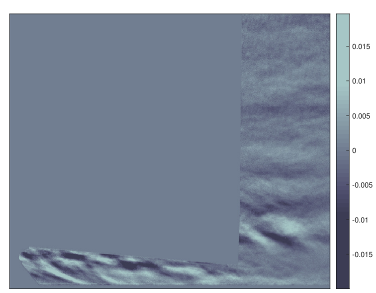

(h) POD mode 21.

Fig. 6 POD mode contours.

B. DMD Modes

The rank truncation in the DMD analysis was set to 21 based on the magnitude of the singular values and the fact that lower energy modes appeared to show less sting interference. The RRMSE value ϵ based on the magnitude of singular values was then 0.04. Standard DMD finds several modes that exhibit a similar pattern depicting sting interference reaching the base flow. However, the DMD spectrum contains eigenvalues that are much less than unity in magnitude. This could suggest that the modes found have a noise-corrupted spectrum. It is well-known that standard DMD is highly sensitive to the presence of random noise. It is argued in [6] that this can reduce the magnitudes of the DMD eigenvalues, leading to errors in frequency and growth rate. The growth rate computation is especially sensitive to noise. Thus, although the DMD modes do have frequencies that come close to those given in the PSD plots above, a definitive comparison of the DMD spectrum and the power spectrum obtained from the POD time coefficients is difficult. The complex conjugate pairs of modes and their associated frequencies could represent vortex shedding or general oscillatory behavior of disturbances originating from the sting and their harmonics, and inspection of the spatial modes suggests this as well. The DMD eigenvalues are plotted with the complex unit circle in Fig. 8 below. The normalized absolute value of amplitude is plotted against associated frequencies and growth rates in Fig. 7. In addition, the 4 modes that most closely depict the sting disturbance are given in Fig.9 below. The modes are multiplied by their associated amplitude before plotting.

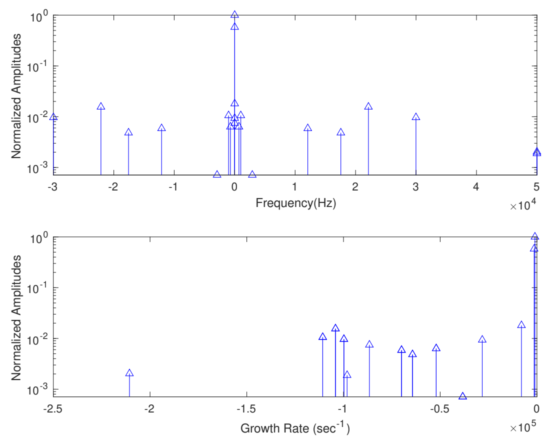

Fig. 7 Normalized DMD amplitude vs frequencies and growth rates.

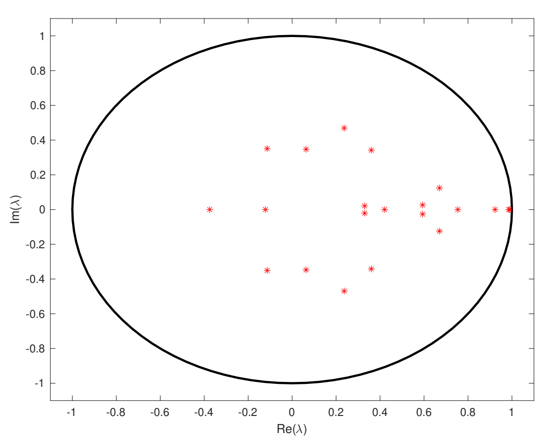

Fig. 8 DMD eigenvalues.

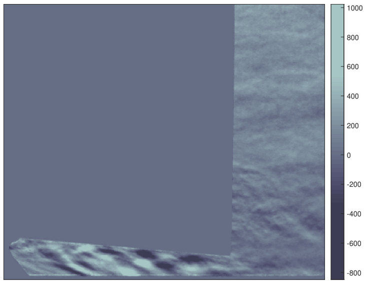

(a) Real part of DMD mode 4.

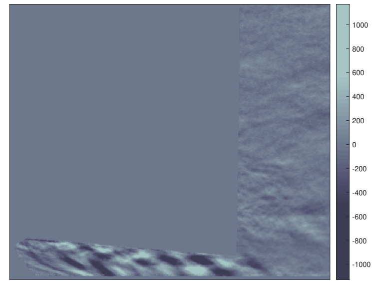

(b) Imaginary part of DMD mode 4.

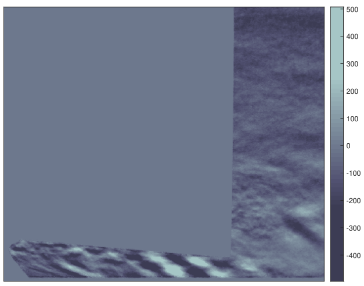

(c) Real part of DMD mode 6.

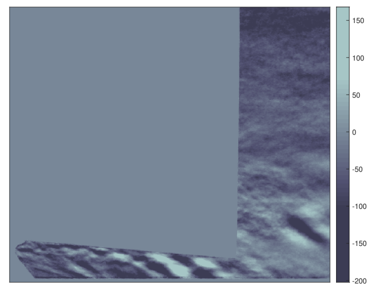

(d) Imaginary part of DMD mode 6.

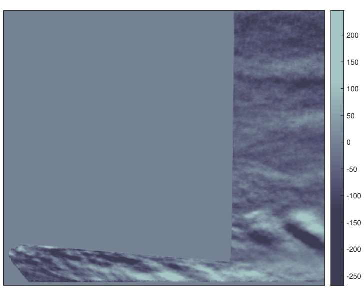

(e) Real part of DMD mode 12.

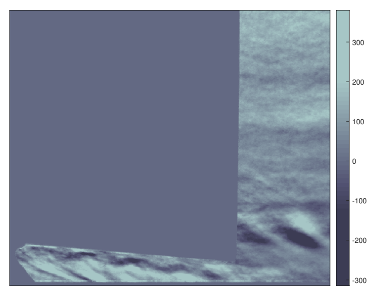

(f) Imaginary part of DMD mode 12.

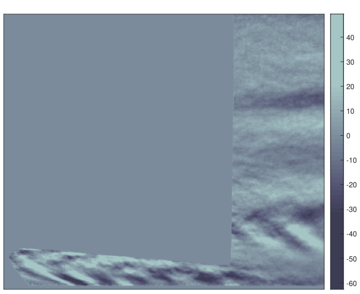

(g) Real part of DMD mode 20.

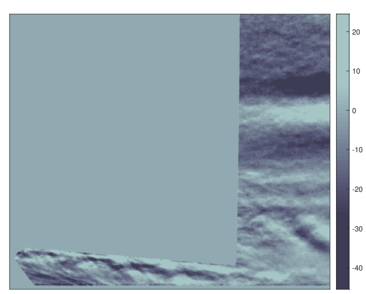

(h) Imaginary part of DMD mode 20.

Fig. 9 DMD modes scaled by their amplitudes.

C. HODMD Modes

The results presented here are for $K = 1000$ snapshots, $\varepsilon = 0.04$, and a delay parameter value of $d = 300$. This value of ε keeps 21 temporal HOSVD modes. The HODMD algorithm found more modes that show points behind the sting having the same frequency and growth rate in the base flow, showing the potential influence of the sting interference downstream. The actual number of modes found with these parameters was 208. The initial HOSVD kept 21 temporal modes and then the DMD-d algorithm decomposed this into 208 modes to keep the RRMSE of the expansion below ε.

The frequencies and growth rates from the initial HODMD analysis are given below in Fig. 10 below. Each arrow represents a single mode and the modes are ordered in terms of descending amplitude. Thus, the first mode is the tallest arrow, seen in both the frequency and growth rate plots with a value of zero for both. Noise present in experimental data has the effect of moving the DMD eigenvalues further inside the unit circle [6]. This is seen in the larger negative growth rates in the standard DMD analysis (Fig. 7). Despite this, the HODMD algorithm finds modes whose eigenvalues are very close in magnitude to unity. This likely represents permanent or minimally damped oscillating dynamics as an eigenvalue with an absolute value of unity signifies zero growth rate, or pure oscillation in time. Thus, the data is represented by modes with potentially more relevant frequencies than the standard DMD analysis gives. The HODMD eigenvalues are plotted with the complex unit circle in Fig. 11 below.

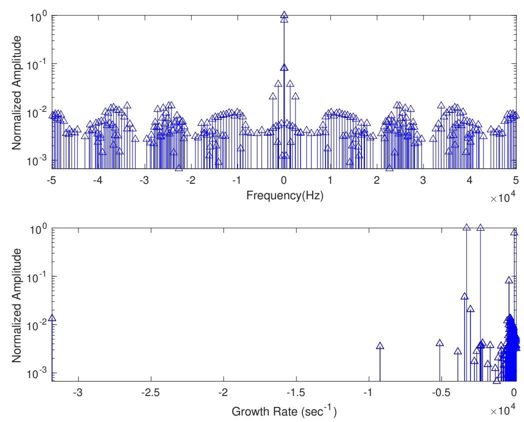

Fig. 10 HODMD frequencies and growth rates.

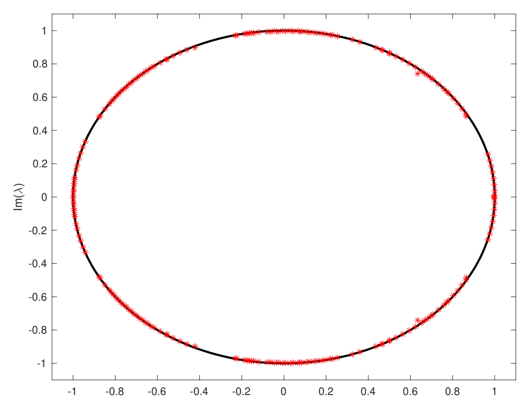

Fig. 11 HODMD eigenvalues.

Some of the HODMD modes are shown below in Figs. 12 and 13. Virtually all of the modes appear to show the interference from the sting, so the highest-amplitude modes whose real or imaginary part shows this most clearly are given here. The mode number given is the n from the DMD expansion, but the modes come in complex conjugate pairs.

Therefore, mode 3 for example is the complex conjugate of mode 2 rather than an entirely different mode. Then mode 5 is the complex conjugate of mode 4 and the mode 4-5 pair is the second distinct complex conjugate pair. The first mode is real-valued mean flow so it does not have the conjugate.

(a) Real part of HODMD mode 5.

(b) Real part of HODMD mode 9.

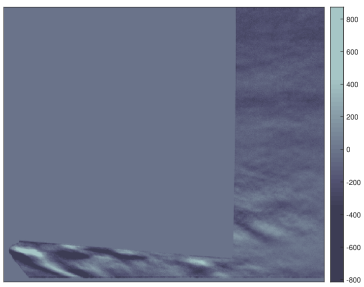

(c) Real part of HODMD mode 11.

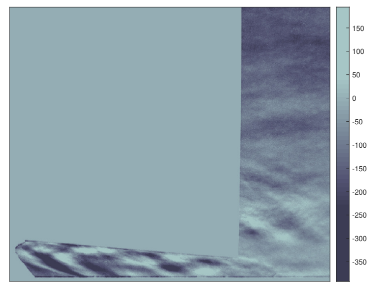

(d) Real part of HODMD mode 15.

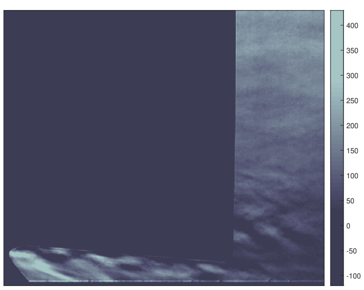

(e) Real part of HODMD mode 17.

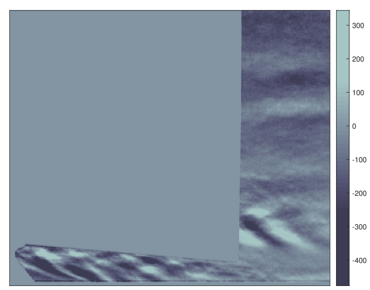

(f) Real part of HODMD mode 31.

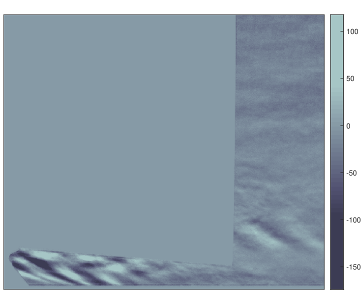

(g) Real part of HODMD mode 33.

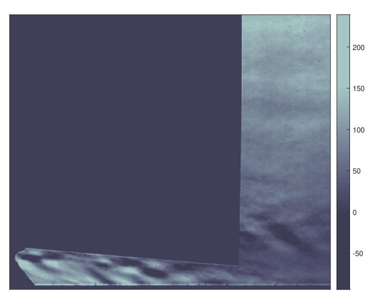

(h) Real part of HODMD mode 37.

Fig. 12 Real part of HODMD modes scaled by their amplitudes.

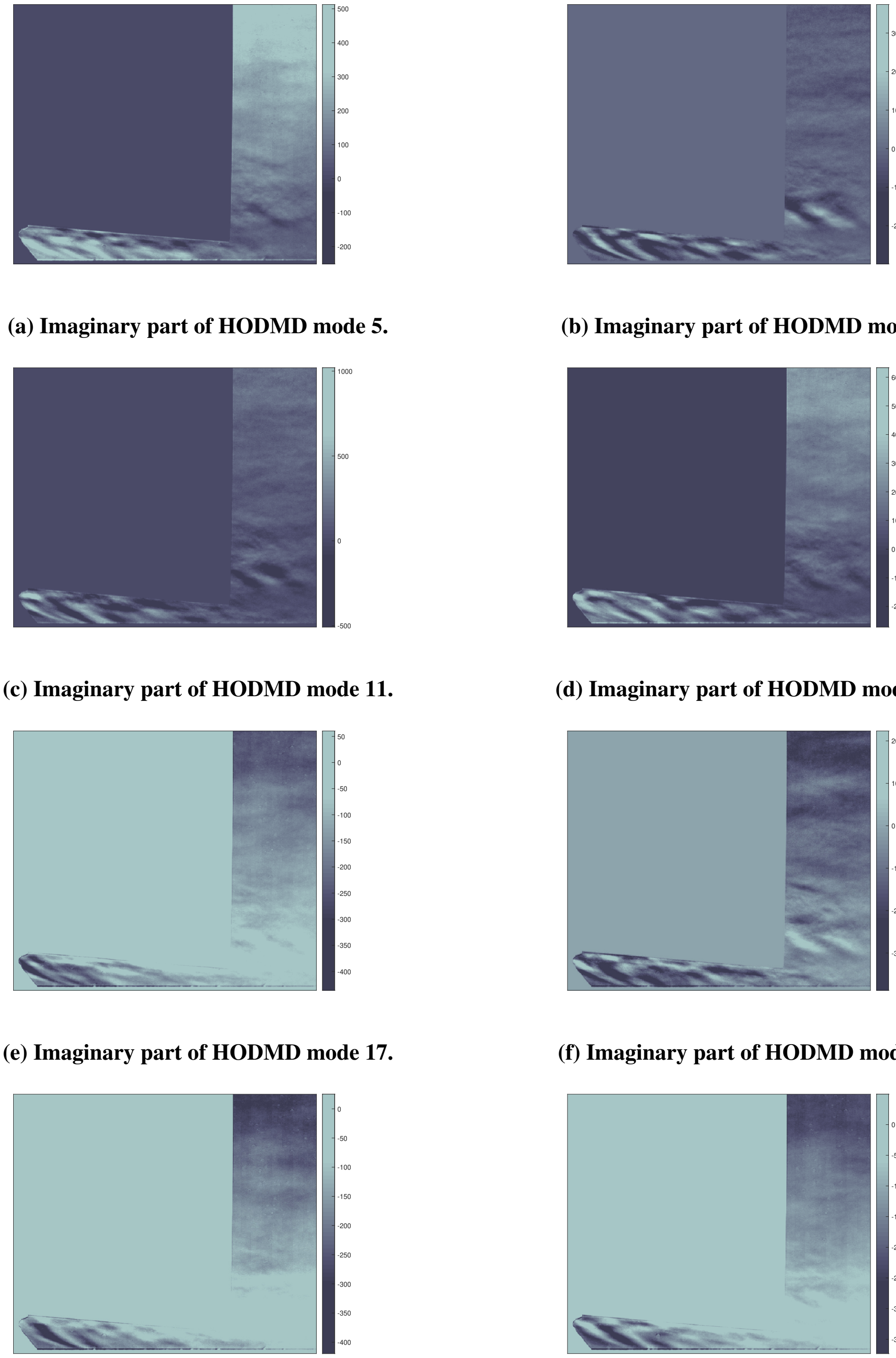

(a) Imaginary part of HODMD mode 5.

(b) Imaginary part of HODMD mode 9.

(c) Imaginary part of HODMD mode 11.

(d) Imaginary part of HODMD mode 15.

(e) Imaginary part of HODMD mode 17.

(f) Imaginary part of HODMD mode 31.

(g) Imaginary part of HODMD mode 33.

(h) Imaginary part of HODMD mode 37.

Fig. 13 Imaginary part of HODMD modes scaled by their amplitudes.

The HODMD analysis computes more modes showing the interference convecting to the base region than DMD. The higher-amplitude HODMD modes that show this influence on the base region could result from the application of HOSVD and the higher-order assumption (Eq. 18) finding relevant dynamics better from the experimental data which contain inherent noise. The improvement of HODMD over DMD is evident because it finds more modes showing base-flow influence and the growth rates are smaller. For analyzing the effect of the sting, it is desirable to find permanent modes rather than transients that rapidly decay. This is because it is difficult to decipher whether rapidly decaying modes persist in different realizations of the same experiment or if they are spurious due to noise or random additional environmental factors. The HODMD method leads to potentially lower errors in computed frequencies due to the higher-order assumption and seems to be more robust to the application of the present schlieren video.

V. Conclusions

We have reviewed three modal decomposition techniques and their applications in analyzing schlieren video. The results from applying these algorithms to schlieren video of Mach 6 flow past a cone model to analyze sting interference have been given. The HODMD algorithm appears to be more robust in finding persisting dynamics from limited experimental data, as expected. The HODMD mode contours show that HODMD has predicted more frequencies associated with the sting interference in the base region than standard DMD. This is partly because noise elimination via the standard DMD with SVD rank truncation limits the number of modes that can be predicted. The temporal complexity of the data necessitates more modes to represent it than is possible with the rank truncation necessary to remove noise. The HODMD method gets around this limitation with the HOSVD along with the delay parameter d. This allows the application of HODMD to pull out potentially more-relevant frequencies from flow visualization data like schlieren videography where standard DMD can be sensitive to noise and give spurious results. The result of the HODMD is spatial modes that resemble coherent flow structures like the POD but with single frequencies in time and smaller decay rates than standard DMD, meaning more persistent dynamics. All methods appear to give some insight into the dynamics involved with the sting interference and suggest the presence of vortex shedding-like disturbances and acoustic propagation that enters the base flow region due to the presence of the sting. Future work plans will involve comparing with experimental base pressure measurements and applying the HODMD in space to gain a better understanding of the disturbance propagation in space that is implicitly described by the HODMD mode contours.

Acknowledgments

This work was supported by AFOSR Grant FA9550-21-1-0432. We are greatful for discussions on the application of modal decomposition methods to experimental schlieren with Dr. Rajan Kumar and Noah Moffeit at Florida State University.

References

[1] Brunton, B. W., Johnson, L. A., Ojemann, J. G., and Kutz, J. N., "Extracting Spatial–Temporal Coherent Patterns in Large-Scale Neural Recordings Using Dynamic Mode Decomposition," *Journal of Neuroscience Methods*, Vol. 258, 2016, pp. 1–15. doi:10.1016/j.jneumeth.2015.10.010, URL `https://doi.org/10.1016/j.jneumeth.2015.10.010`.

[2] Weiss, J., "A Tutorial on the Proper Orthogonal Decomposition," 2019. doi:10.14279/DEPOSITONCE-8512, URL `https://depositonce.tu-berlin.de/handle/11303/9456`.

[3] Towne, A., Schmidt, O. T., and Colonius, T., "Spectral Proper Orthogonal Decomposition and its Relationship to Dynamic Mode Decomposition and Resolvent Analysis," *Journal of Fluid Mechanics*, Vol. 847, 2018, pp. 821–867.

[4] Kutz, J. N., Brunton, S. L., Brunton, B. W., and Proctor, J. L., *Dynamic Mode Decomposition: Data-Driven Modeling of Complex Systems*, SIAM, 2016.

[5] Schmid, P. J., and Sesterhenn, J., "Dynamic Mode Decomposition of Experimental Data," *8th International Symposium on Particle Image Velocimetry, Melbourne, Victoria, Australia*, 2009.

[6] Dawson, S. T., Hemati, M. S., Williams, M. O., and Rowley, C. W., "Characterizing and Correcting for the Effect of Sensor Noise in the Dynamic Mode Decomposition," *Experiments in Fluids*, Vol. 57, 2016, pp. 1–19.

[7] Clainche, S. L., and Vega, J. M., "Higher Order Dynamic Mode Decomposition to Identify and Extrapolate Flow Patterns," *Physics of Fluids*, Vol. 29, No. 8, 2017, p. 084102. doi:10.1063/1.4997206, URL `https://doi.org/10.1063/1.4997206`.

[8] Clainche, S. L., and Vega, J. M., "Spatio-Temporal Koopman Decomposition," *Journal of Nonlinear Science*, Vol. 28, No. 5, 2018, pp. 1793–1842. doi:10.1007/s00332-018-9464-z, URL `https://doi.org/10.1007/s00332-018-9464-z`.

[9] Lamb, J. P., and Oberkampf, W. L., "Review and Development of Base Pressure and Base Heating Correlations in Supersonic Flow," *Journal of Spacecraft and Rockets*, Vol. 32, No. 1, 1995, pp. 8–23.

[10] Price, B. N., McDaniel, Z. A., Miller, S. A., Overpeck, S. J., Lavery, N. T., and Jewell, J. S., "High-Speed Schlieren Visualization in Mach-6 Quiet Tunnel," *AIAA SciTech*, San Diego, CA, 2022. doi:10.2514/6.2022-1672.

[11] McDaniel, Z. A., Price, B. N., Miller, S. A., and Jewell, J. S., "Boundary-Layer Analysis in Mach-6 Quiet Tunnel Using Schlieren Methods," *AIAA Aviation*, Chicago, IL, 2022. doi:10.2514/6.2022-3531.

[12] Mamrol, D. V., and Jewell, J. S., "Freestream Noise in the Purdue University Boeing/AFOSRMach-6 Quiet Tunnel," *AIAA SciTech*, San Diego, CA, 2022. doi:10.2514/6.2022-2453.

[13] Miller, S. A., Redmond, J. J., Jantze, K., Scalo, C., and Jewell, J. S., "Investigation of Second-Mode Instability Attenuation Over Porous Materials in Mach-6 Quiet Flow," *AIAA Aviation*, Chicago, IL, 2022. doi:10.2514/6.2022-3530.

[14] Miller, S. A., Redmond, J. J., Jantze, K., Scalo, C., and Jewell, J. S., "Investigation of Second-Mode Instability Attenuation Over Silicon-Carbide Coated Carbon Foam," *AIAA Aviation*, San Diego, CA, 2023. doi:10.2514/6.2023-4203.

[15] McDaniel, Z. A., and Jewell, J. S., "Application of Schlieren Methods to Flared Cone in Mach-6 Quiet Tunnel," *AIAA SciTech*, Orlando, FL, 2024.

[16] Benitez, E., Borg, M., Paredes, P., Schneider, S., and Jewell, J., "Measurements of an Axisymmetric Hypersonic Shear-Layer Instability in Quiet Flow," *Physical Review Fluids*, Vol. 8, No. 8, 2023, p. 083903. doi:10.1103/PhysRevFluids.8.083903.

[17] Benitez, E., Borg, M., Scholten, A., Paredes, P., McDaniel, Z., and Jewell, J., "Instability and Transition Onset Downstream of a Laminar Separation Bubble at Mach 6," *Journal of Fluid Mechanics*, Vol. 969, 2023, p. A11. doi:10.1017/jfm.2023.533.

[18] Francis, A. A., Dylewicz, K., Klothakis, A., Theofilis, V., and Jewell, J. S., "Instability Measurements on a Cone-Slice-Flap in Mach-6 Quiet Flow," *AIAA SciTech*, Orlando, FL, 2024.

[19] Francis, A. A., and Jewell, J. S., "Effect of Angle of Attack on Separation Bubble Instability and Transition on a Cone-Slice-Ramp in Mach-6 Quiet Flow," *AIAA SciTech*, Orlando, FL, 2024.

[20] Noftz, M. E., Shuck, A. J., Jewell, J. S., Poggie, J., Bustard, A., J., J. T., and Bisek, N. J., "Performance Evaluation of an Internal Osculating Waverider Inlet," *AIAA SciTech*, National Harbor, MD, 2023. doi:10.2514/6.2023-4203.

[21] Brunton, S. L., Kutz, J. N., Brunton, B., and Proctor, J. L., "Dynamic Mode Decomposition," , 2016. URL `hhttp://www.dmdbook.com/`, accessed on April 18, 2023.

[22] Corrochano, A., D'Alessio, G., Parente, A., and Clainche, S. L., "Higher Order Dynamic Mode Decomposition to Model Reacting Flows," 2022. doi:10.48550/ARXIV.2203.11574, URL `https://arxiv.org/abs/2203.11574`.